Pergamon

Int. J. Heat Mass Transfer. Vol. 40, No. 12, pp. 2799–2812, 1997

Printed in Great Britain
0017–9310/97 $17.00+0.00

PII: S0017–9310(96)00335–3

Steady natural convection in a two-layer system of immiscible liquids

A. PRAKASH† and J. N. KOSTER‡

Department of Aerospace Engineering Sciences, Boulder, University of Colorado, CO 80309-0429, U.S.A.

(*Received* 20 *December* 1995 *and in final form* 19 *September* 1996)

Abstract—Thermal convection in two horizontal layers of immiscible liquids that are differentially heated from the side is studied analytically, numerically and experimentally. The flow in the two layers is thermally and mechanically coupled. Flow in both layers is visualized and the flow pattern is found to be in agreement with theoretical predictions. Flow velocities in the core region of the cavity are found to be in quantitative agreement with theory. © 1997 Elsevier Science Ltd.

INTRODUCTION

The study of thermal convection in a two-layer system of immiscible liquids is inspired by the development of liquid encapsulated crystal growth techniques. Encapsulation is used to control melt stoichiometry when the melt contains a volatile component. The encapsulant, typically a liquid glass, also has the potential for reducing, or even eliminating, convective flow in the melt. Convection in the melt, especially time-dependent flow, is considered a source of undesirable inhomogeneities in the solidified material. Fluid dynamics of an electronic melt during the solidification process involves the transport of mass and heat, as well as a phase change. Therefore, we consider the basic dynamics of a simplified model: a differentially heated immiscible two-layer system featuring a liquid/liquid interface and a free upper surface.

The two-layer convection problem is an extension of the broadly studied problem of natural convection in a differentially heated cavity with a single liquid that is either completely confined, or features a free surface. Batchelor [1] investigated the confined problem. For a small driving force, as measured by the Grashof number Gr, his solution is an asymptotic expansion about the purely conductive, constant temperature gradient solution. For large Gr numbers, he predicts an isothermal core, with thin boundary layers along all four sides. Gill [2] studied the large Gr number problem for the case of large aspect ratio cavities ($d/L \gg 1$, where d is the layer height and L the horizontal extension). He predicts a flow within thin boundary layers along the heated side walls where almost all the temperature drop occurs and a core region where the temperature is not isothermal as in Batchelor's solution, but is a function of the vertical coordinate.

Several investigators have since studied this "cavity" problem numerically [3, 4]. Cormack *et al.* [5], Cormack *et al.* [6] and Imberger [7], hereafter collectively referred to as CLI, investigated single layer convection in a shallow cavity with $d/L \ll 1$. They present an asymptotic theory valid in the limit $d/L \to 0$, with a fixed Gr. They also present experimental and numerical results that show excellent agreement with theory. Sen and Davis [8], hereafter referred to as SD, utilized a similar asymptotic analysis to study thermocapillary convection in a single layer with a free surface, and with both surfaces free. SD included the effect of a deformable interface in their analysis. Prakash and Koster [9, 10] extended the asymptotic analyses of CLI and SD to multi-layer systems.

Villers and Platten [11, 12] performed a one-dimensional (1-D) analysis of convective flow in a two-layer system. They assumed that the temperature gradient across the cavity is constant, and a parallel flow with negligible vertical velocity develops in both layers. By using the LDV technique (laser Doppler velocimetry), Villers and Platten have also measured flow velocities in low speed thermal convective flows in single layers, and in two-layer systems. Ramachandran [13], and Doi and Koster [14] utilized finite difference algorithms, while Fontaine and Sani [15] used the finite element code FIDAP to numerically simulate the flow in two-layer systems with a free surface. Doi and Koster predict a "halt condition" for the lower layer, whereby judicious selection of the encapsulating upper layer, flow in the lower layer is halted.

CLI and SD have shown that, in shallow cavities, with aspect ratios $d/L \ll 1$, the flow can be divided into three horizontally adjacent regions: the central or "core" region, and the two end regions where flow turns around. Flow in the "core region" is considered parallel to the interfaces, i.e. vertical velocity com-

---

† Currently at NASDA, Space Utilization Dept., Tsukuba City, Japan.

‡ Author to whom correspondence should be addressed.

NOMENCLATURE

A	liquid layer aspect ratio
A_n	integration constants ($n = 0$–4)
Bd_d, Bd_s	dynamic, static Bond numbers
C_n, C_n^*	integration constants ($n = 1, 2, 3, \ldots$)
C	capillary number
d	individual layer height
D	cavity horizontal depth
f	arbitrary field variable used for defining operator $\langle \ldots \rangle$
$f(y)$	vertical variation of streamfunction in the core region
$g(y)$	vertical variation of temperature in the core region
g	gravitational acceleration
h	surface deformation
H	test-cell height
$K_{1,2}$	integration constants
L	test-cell width
p	pressure
Pr	Prandtl number
Gr	Grashof number
T	temperature
u	velocity
x, y	horizontal, vertical coordinates.

Greek symbols

α	thermal expansion
γ	surface tension
θ	non-dimensional temperature
κ	thermal diffusivity
λ	thermal conductivity
μ	dynamic viscosity
ρ	density
σ_0	surface tension
ν	kinematic viscosity
ω	vorticity
Ψ	stream-function
ξ	stretched horizonal coordinate in the end-region
η	stretched vertical coordinate in the end-region.

Subscripts

b	bottom
t	top
i	interface
s	free surface
n	order in the asymptotic expansion ($n = 0, 1, 2, 3, \ldots$).

Superscripts

B	ratio of properties—b/b (equals unity)
T	ratio of properties—t/b
$\pm$j	layer above/below surface
i	layer numbering (t/b or T/B)
S	ratio of properties—s/i
S	non-dimensional surface deformation
I	ratio of properties—i/i (equals unity)
I	non-dimensional interface deformation.

ponents are negligible. The horizontal temperature profile in the core region is linear at all vertical locations. The entire temperature drop occurs across the core region. The end regions only serve to turn the flow around and play a passive role with regards to heat transfer. This is in contrast to the case where most of the temperature drop occurs in vertical thermal boundary layers at the end-walls, while the horizontal temperature gradient in the core region is small and negligible. Shallow cavities are therefore particularly well suited for the study of thermocapillary flow, which relies on the horizontal temperature gradient for its driving force. In this study we restrict our focus to shallow cavities.

A characteristic feature of the multi-layer problem is the coupling across liquid/liquid interfaces. The liquid layers are mechanically coupled via transfer of momentum across the interfaces. Transfer of momentum results from the continuity of interface tangential velocity, and from a stress balance across the interface. Together these two conditions comprise the "no-slip" condition at a liquid–liquid interface. Thermal coupling is achieved through continuity of temperature and balance of heat transfer across the interface. The terms thermal and mechanical coupling were profferred by Honda [16] in the context of Rayleigh–Bénard convection in layered systems. The two layers are identified as "thermally coupled" when circulation rolls in the two layers are co-rotating, i.e. the flow has the same sense of rotation in both layers. On the other hand, the layers are considered "mechanically coupled" if the circulation rolls are counter-rotating, i.e. flow along the interface is in the same direction in both layers. In this case, fluid in one layer mechanically drags the fluid in the other layer. This implies that regions of ascending hot fluid in one layer coincide with regions of descending cold fluid in the other layer. Viscous drag across the interface forces the two fluids to flow in the same direction.

In the current state of research on multi-layer convection, experimental validation of the theory is at-best ambiguous. While thermal coupling is presumed to hold, the transfer of momentum appears to be inoperative for some liquid combinations. It has been suggested that the transfer of momentum is impeded by the presence of interfacial contaminants in the form of monolayers or interfacial viscosity. In such an event, the fluid at the interface is immobile and the interface behaves as a rigid membrane separating layers. Such incongruities have been reported for bilayer convection in systems heated from below [17, 18]. Villers *et al.* [11] measured the velocity profile at the center of the side-heated cavity and reported good qualitative agreement with their 1-D analysis. However, the velocity at the interface was found to be very near zero and evidence of a clear interfacial region is vague. Azuma *et al.* [19] observed an interfacial flow region indicating a mechanically coupled flow. They report qualitative agreement with 2-D numerical simulations.

Here, we present a study of thermal convection in two-layers which parallels CLI's exhaustive investigation of single layer convection in a shallow cavity. We report results from flow visualization experiments, along with flow velocity measurements. The experimental results are compared with two-dimensional (2-D) numerical simulations. The results are also compared with an extension of CLI and SD's analytical model to two-layer systems.

EXPERIMENTAL SETUP

Experiments are performed in a two-layer system: 10 cSt silicone oil over a fluorinert FC-70 liquid. These liquids are selected because of their mutual immiscibility and their resistance to surface and interfacial contamination. The liquid combination is considered immiscible because diffusion in the form of Schlieren was not detected under monochromatic laser light. Thermophysical properties for the liquids and pertinent ratios are shown in Tables 1 and 2, respectively.

The test cell configuration is shown in Fig. 1. The fluid test volume is a rectangular cavity with a length between the temperature controlled side walls $L = 38$ mm, height $H = 28.5$ mm and side wall separation in the viewing direction $D = 28.5$ mm. The cavity is filled with the two liquids such that each liquid layer height is $d = 6$ mm. The vertical side walls of the test volume are copper. They provide the isothermal boundary conditions. The test cell bottom is PVC which approaches an adiabatic boundary. The top of the cavity is Plexiglas. It insulates the cavity from the outer environment while allowing for the transmission of a light sheet for flow visualization. The front and back walls are window glass. The test cell is thermally insulated with phenolic frames. The glass windows are covered with foam insulation which is periodically removed for visualization.

Temperature control is achieved by circulating coolant through channels drilled in the copper sidewalls. Temperature stability in the test cell is further improved by passing the coolant through insulated brass blocks ("thermal buffers") before entering the test cell. Thermocouples are placed within 2 mm of the copper–fluid interface to measure the ΔT across the test cell. Accuracy of ±0.05°C in the temperature

Table 1. Fluid properties

Fluids	Density ρ (g cm^{-3})	Kinematic viscosity ν cm^2 s^{-1})	Dynamic viscosity μ (g cm^{-1} s^{-1})	Thermal conductivity λ (W cm^{-1} K^{-1})	Specific heat c_p (J g^{-1}K^{-1})	Thermal diffusivity κ (cm^2 s^{-1})	Coeff. of expansion α (K^{-1})	Prandtl number Pr 1	Surface tension σ (dy cm^{-1})	Surface tension gradient γ (dy cm^{-1} k^{-1})
FC70	1.94	0.134	0.26	7.00×10^{-4}	1.05	3.44×10^{-4}	1.00×10^{-3}	390	19.7	−0.06
SO 10cSt	0.935	0.1	0.0935	1.34×10^{-3}	1.51	9.51×10^{-4}	1.10×10^{-3}	105	18.6	−0.067

Table 2. Ratio of fluid properties

Two layers	Density ratio	Kinematic viscosity ratio	Dynamic viscosity ratio	Thermal conductivity ratio	Specific heat ratio	Thermal diffusivity ratio	Coeff. of expansion ratio	Prandtl number ratio	Interface tension (dy cm^{-1})	Interface tension gradient (dy cm^{-1} k^{-1})
SO 10cSt/FC70	0.48	0.75	0.36	1.91	1.44	2.76	1.10	0.27	6.90	−0.029

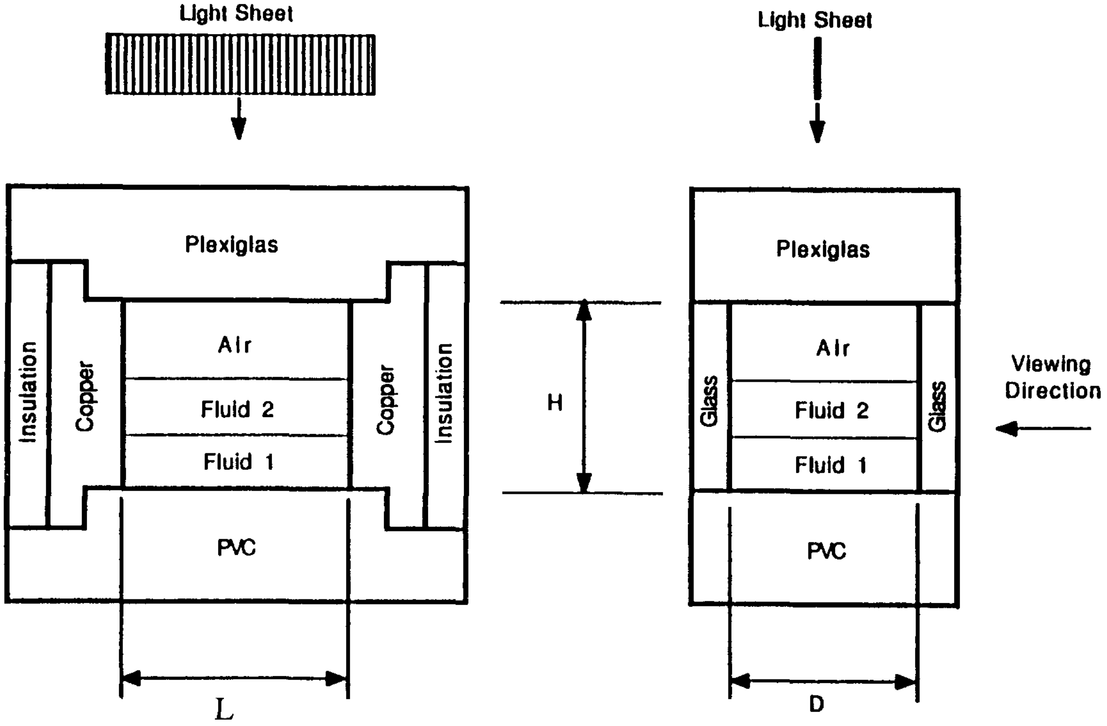

Fig. 1. Schematic of the test cell.

difference measurement is achieved with good confidence. Temperature of the side-wall boundaries is ramped to specific temperature differences [ΔT] at a rate of 0.01 K min^{-1}. The mean temperature is maintained close to room temperature. The liquid layers are allowed to attain thermal equilibrium by maintaining the ΔT constant for a time period larger than twice the thermal diffusion time for either of the two liquids. Then, data is acquired and the ramp is continued to achieve a new ΔT plateau.

The flow field is visualized with the aid of tracer particles suspended in the fluids. The particles are illuminated by a vertical laser light sheet that enters the test-cell from above and is no thicker than 3 mm. The particles used in the experiments are either titanium dioxide flakes ranging in size from 1 to 20 μm, or 60 ± 10 μm diameter silver coated glass microspheres. Movement of the particles with the flow is recorded as streaklines. Single component velocity measurements are performed with a laser Doppler velocimetry (LDV) system [20]. Real time holographic interferometry is used to obtain the temperature field. Detailed description of a real time holographic interferometry set-up may be found in Koster [21]. Because the temperature change is the source of the refractive index change, the fringes in the interferograms are interpreted as isotherms [22].

We also measured the temperature variation of the surface tension and the interface tension for the two liquids under investigation [23]. The measurements were performed using the duNoüy ring method [24]. The interface tension meter is equipped with a temperature controlled chamber, which makes it well suited for measuring surface/interface tension as a function of temperature with an accuracy of ± 0.1 dynes cm^{-1}. The surface tension for both liquids and the interface tension between the liquids decreases with increasing temperature (Tables 1 and 2).

NUMERICAL SIMULATION

Flow in the two-layer system is numerically simulated using the commercial finite element computer code FIDAP. The interface and the free surface are both considered to be deformable. Simulation of the experimental system is restricted to a 2-D model. The 2-D assumption is never completely consistent with an experimental cavity flow. While large cavities lead to 3-D flow, narrow cavities affect the flow through the development of boundary layers and tend to constrain the 3-D flow. Flow in the test cell was evaluated with a horizontal light sheet. We found that flow in the central plane neighborhood can be reliably considered a 2-D flow and can be compared with 2-D numerical simulations.

The governing steady Navier–Stokes equations, the energy equation, the stress balance and the kinematic condition at the free surface and the interface are discretized using the finite element method. The discretized system of nonlinear equations is solved using FIDAP's segregated algorithm. The segregated algorithm, which is based on the implicit approach, discretizes and solves each conservation equation separately in a sequential manner, rather than solving the fully coupled system of equations together. As an explicit matrix equation for pressure does not exist, a Poisson type pressure matrix equation is used in place of the continuity equation. The pressure projection approach is used in this analysis to satisfy the discretized continuity equation. Surface deformations introduce an additional set of degrees-of-freedom. With the segregated algorithm, free surface problems are solved in two steps. First the flow problem is solved by imposing either the kinematic condition or the normal stress balance on the free surfaces. Once convergence of the field variables is attained, the excluded boundary condition is used to determine the movement of the free surface and satisfy the computed flow variables. The procedure is repeated until convergence is attained. For this analysis we iterate on the normal stress condition, i.e. the kinematic constraint is satisfied as part of the flow solution. For a complete description of the discretization procedure and the solution methods available, we refer to the FIDAP users manual [25].

The test cavity is discretized with a nonuniform mesh of 51×71. A finer mesh gradation is utilized in regions where strong velocity and temperature gradients are anticipated. This includes regions near the solid boundaries, as well as the interface and the free surface. This mesh was determined by refining the mesh size until convergence and constancy of maximum streamfunction was achieved (within the limits of available computer resources). As will be discussed in the results section, the mesh refinement was sufficient to capture all the dominant flow structures. The governing equations are solved in dimensional form. The pressure penalty parameter is set to 1.0×10^{-9}. The nonlinear system is iteratively solved until the two convergence criteria for velocity norm and surface deformation norm are satisfied. The convergence criteria for the velocity norm is set to 1.0×10^{-4} and that for the surface norm is set to 1.0×10^{-3}.

An additional constraint on the deformations along the free surface and the interface is that the volume of both liquids must be conserved. The solution is approached in two steps. In the first step, the free surface is held fixed and the interface is deformable. The flow solution and the deformed mesh geometry from this step are used as the starting point for the second step, where the free surface is deformable and the interface is fixed. Thus only one free surface is allowed to deform at one time and volume of both liquids is conserved. For each step, the solution procedure and convergence criteria are as described above. The steps are repeated until the flow solution and deformations become constant.

ANALYTICAL MODEL

We consider a shallow, rectangular, two-dimensional cavity of aspect ratio $H/L \ll 1$. The two layer heights are not necessarily equal, but each layer's aspect ratio is assumed to be small. The total cavity height is, therefore, considered to be much smaller than the cavity length L.

The reader is referred to [9, 10] for details of the 2-D mathematical model for multi-layer systems. The method of matched asymptotic expansions applied to pure buoyancy driven flow in a single layer can be found in CLI [5–7], and that for thermocapillary flow in a single layer in SD [8]. Here, only specifics for the two layer problem are described.

Utilizing the streamfunction-vorticity formulation of the Navier–Stokes equations, the non-dimensional governing equations of fluid flow in each liquid layer [$i = b, t$] are:

$$GrA^2 \frac{\partial(\omega^i, \psi^i)}{\partial(x, y)} = \nu^i \left(A^2 \frac{\partial^2 \omega^i}{\partial x^2} + \frac{\partial^2 \omega^i}{\partial y^2} \right) + \alpha^i \frac{\partial \theta^i}{\partial x} \tag{1}$$

$$A^2 \frac{\partial^2 \Psi^i}{\partial x^2} + \frac{\partial^2 \Psi^i}{\partial y^2} = -\omega^i \tag{2}$$

$$GrPrA^2 \frac{\partial(\theta^i, \Psi^i)}{\partial(x, y)} = \kappa^i \left(A^2 \frac{\partial^2 \theta^i}{\partial x^2} + \frac{\partial^2 \theta^i}{\partial y^2} \right). \tag{3}$$

The governing equations have been scaled using thermophysical properties of the bottom layer, the bottom layer height d, the length of the cavity L and the applied temperature difference ΔT. The following length, velocity, temperature, and pressure scales are used:

$$x^* = L; \quad y^* = d \tag{4}$$

$$u^* = \left(\frac{g\alpha \Delta T d^2}{\nu} \right) \frac{d}{L}; \quad T^* = \Delta T \theta; \quad p^* = \frac{\mu u^* L}{d^2}. \tag{5}$$

Non-dimensional parameters appearing in the above formulation are:

$$A = \frac{d}{L}; \quad Gr = \frac{g\alpha \Delta T d^3}{\nu^2}; \quad Pr = \frac{\nu}{\kappa}. \tag{6}$$

As noted earlier, the layer heights do not need to be equal. However, in the following, the aspect ratios of the two layers are assumed to be the same order. This allows the same ordering parameter A to be used in the asymptotic expansions for both layers. Superscripts denote ratios of thermophysical properties, i.e.

$$\nu^{\mathrm{T}} = \frac{\nu_t}{\nu_b}. \tag{7}$$

The surface tension σ_0 and its temperature gradient γ are scaled using the interface values, as follows

$$\gamma^{\mathrm{S}} = \frac{\gamma_s}{\gamma_i}; \quad \sigma_o^{\mathrm{S}} = \frac{\sigma_{os}}{\sigma_{oi}}; \quad \gamma^{\mathrm{I}} = 1; \quad \sigma_o^{\mathrm{I}} = 1. \tag{8}$$

Also, surface and interfacial deformations are scaled using the bottom layer height d,

$$h^{S}(x) = \frac{h^{S}(x)}{d}; \quad h^{I}(x) = \frac{h^{i}(x)}{d}. \tag{9}$$

At the rigid side walls and the bottom boundary the flow boundary conditions are the no-slip conditions. At the cold and hot side-walls, an isothermal condition applies and the bottom is adiabatic. These conditions are:

$$(x = 0,1): \quad \begin{cases} \Psi^{i} = \Psi^{i}_{x} = 0; & h^{j}(x) = 0 \\ \theta^{i} = 0(x = 0); & \theta^{i} = 1(x = 1) \end{cases} \tag{10}$$

$$(y = 0): \quad \Psi^{i} = \Psi^{i}_{y} = 0; \quad \theta^{i}_{y} = 0. \tag{11}$$

At the free surface and the interface, the boundary conditions are continuity of velocity and temperature, the kinematic condition, balance of normal and shear stress and heat flux balance. Unlike the analysis of SD, in this analysis it is important to include the effect of hydrostatic pressure in the normal stress balance at the free surface and at the interface. The boundary conditions take the form:

$$(y = 1+h^{I}, 1+d^{T}+h^{S}):$$

$$\Psi^{-j}_{x} = \Psi^{+j}_{x} = 0; \quad \Psi^{-j}_{y} = \Psi^{+j}_{y} = 0 \tag{12}$$

$$\Psi^{-j}_{x} + h^{j}_{x}\Psi^{-j}_{y} = \Psi^{+j}_{x} + h^{j}_{x}\Psi^{+j}_{y} = 0 \tag{13}$$

$$\begin{aligned} -\langle p\rangle + \frac{2A^{2}}{(1+A^{2}h^{j^{2}}_{x})}\langle \mu[-(\Psi_{xy} + h^{j}_{x}\Psi_{yy}) \\ + A^{2}h^{j}_{x}(h^{j}_{x}\Psi_{xy} + \Psi_{xx})]\rangle \\ = \frac{A^{3}h^{j}_{xx}}{C(1+A^{2}h^{j^{2}}_{x})^{3/2}}\left(\sigma^{j}_{o} - \frac{1}{A}\frac{C}{Bd_{d}}\gamma^{j}\theta^{j}\right) \\ + A\frac{Bd_{s}}{C}h^{j} - \langle\rho\alpha\rangle 0h^{j} - \theta_{y}h^{j^{2}} \end{aligned} \tag{14}$$

$$\begin{aligned} \langle \mu[(1 - A^{2}h^{j^{2}}_{x})(\Psi_{yy} - A^{2}\Psi_{xx}) - 4A^{2}h^{j}_{x}\Psi_{xy}]\rangle \\ = -\frac{1}{Bd_{d}}\gamma^{j}(1+A^{2}h^{j^{2}}_{x})^{1/2}(\theta^{j}_{x} + h^{j}_{x}\theta^{j}_{y}) \end{aligned} \tag{15}$$

$$\langle \lambda[\theta_{y} - A^{2}h^{j}_{x}\theta_{x}]\rangle = 0 \tag{16}$$

where the operator $\langle \ldots \rangle$ is defined as,

$$\langle f\rangle \equiv f^{-j} - f^{+j}. \tag{17}$$

The additional non-dimensional parameters in the above boundary conditions are C, Bd_{s} and Bd_{d}. These are defined using the interface tension and interface tension gradient, along with thermophysical properties and layer height of the bottom layer as follows:

$$C = \frac{u^{*}\mu}{\sigma_{0}}; \quad Bd_{d} = \frac{\rho\alpha g d^{2}}{\gamma}; \quad Bd_{s} = \frac{(\rho_{b} - \rho_{t})gd^{2}}{\sigma_{0}}. \tag{18}$$

Additionally, we have the conservation conditions,

$$(y = 1+h^{I}, 1+d^{T}+h^{S}): \quad \Psi^{-j} = \Psi^{+j} = 0 \tag{19}$$

$$\int_{1/2}^{1/2} h^{j}(x)\,\mathrm{d}x = 0. \tag{20}$$

To proceed further with the asymptotic expansion, an estimate of the order of magnitude of the non-dimensional parameters characterizing the flow (Gr, Bd_{d} and C) is required. We proceed with the development of CLI and SD and assume the flow to be "slow", i.e. $Gr \sim O(1)$. The above limitation on capillary number is discussed by SD. Additionally, we assume that,

$$C = \bar{C}A^{4}; \quad ABd_{s} = \overline{Bd_{s}};$$

$$Pr \sim Bd_{d} \sim \bar{C} \sim \overline{Bd_{s}} \approx O(1). \tag{21}$$

The objective is to solve the above system of equations in the two layers with the applicable boundary conditions in the limit $A \to 0$. As shown by CLI and SD, the solution proceeds by expanding the field variables using the small parameter A and formulating the governing equations and boundary conditions at different orders of A. The solution approach is delineated in refs. [9, 10]. The key distinction here is that the system is (1) composed of two layers; (2) that both buoyancy and thermocapillary effects are included in this formulation; (3) surface and interfacial deformations are included; (4) both the hot and cold end walls are considered. For the assumed slow flow, it is clear from equation (14) that the hydrostatic pressure limits the deformations to be at most $O(A^{4})$. The resulting equations in the core region, and in the cold and hot end regions, along with the boundary conditions at each order of the expansion are available from the corresponding author upon request.

RESULTS

Results from the analytical method are calculated for the conditions of the accompanying experiment. At $O(1)$, the flow is composed of a single roll in each layer and the flow in the two end-regions is perfectly mirror symmetric. The end-walls only serve to turn the flow around. The layers are mechanically coupled via a very thin roll above the interface. Flow in this interfacial roll is much slower than flow in the bulk of the layer. At $O(A)$ the flow is affected by thermocapillary stresses along the free surface and along the interface. The flow is no longer mirror symmetric and is distorted by the interfacial roll.

End-region streamlines correct to $O(A^{2})$ are shown in Fig. 2(a). Symmetry in the two end-regions is further broken at this order. The single roll flow structure in the upper layer is modified by the presence of a stronger interfacial roll. The interfacial roll thickness is largest in the end-regions, and reduces as the core region is approached. At the hot wall the interfacial roll is thicker than at the cold wall and includes a substantial internal recirculation. Streamlines at this order are considered to have full physical relevance.

The physically relevant order for the temperature

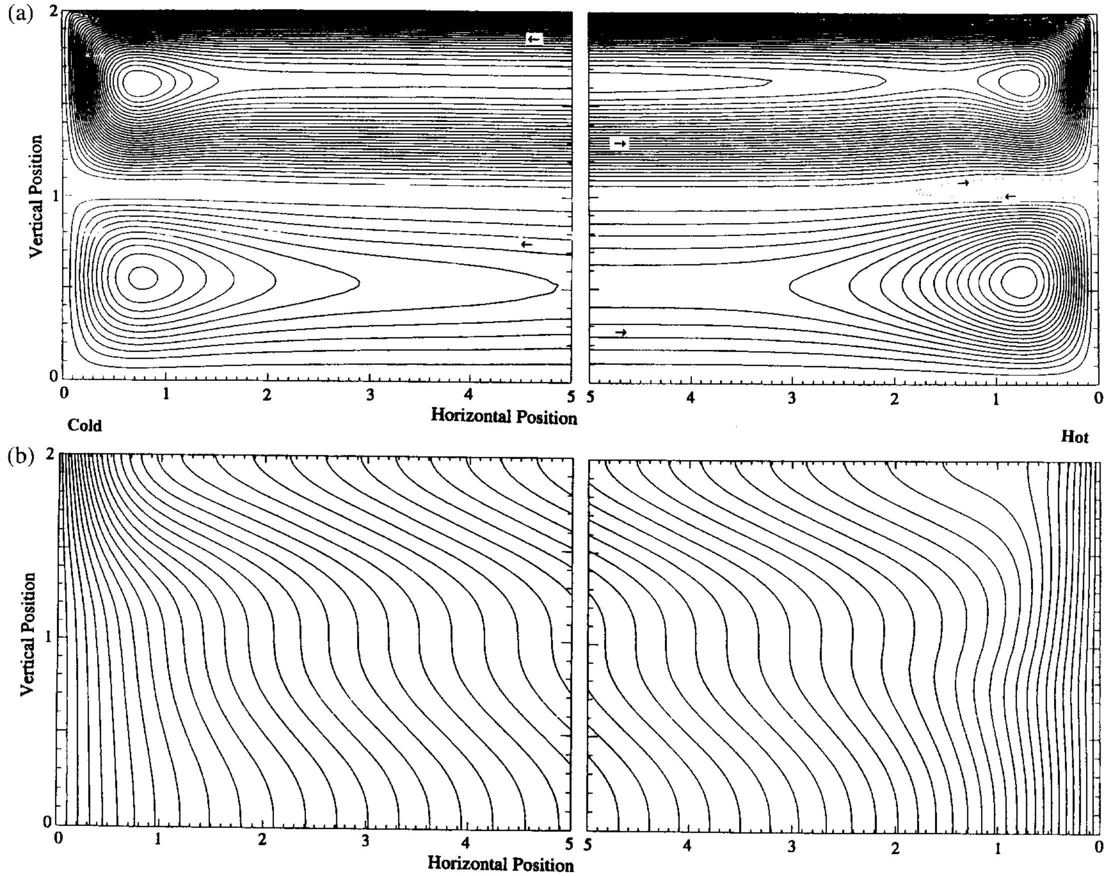

Fig. 2. (a) Flow streamlines at O(A^2), $Gr = 10$, $Bd_d = 23.6$, $A = 0.16$; (b) temperature contours at O(A^3), $Gr = 10$, $Bd_d = 23.6$, $A = 0.16$.

field corresponding to the streamlines at O(A^2) is the temperature field at O(A^3) [9, 10]. Temperature contours, correct to O(A^3), for the two end-regions are shown in Fig. 2(b). Isotherms in both layers are significantly deformed by the flow. The formation of thermal boundary layers at the two end-walls is apparent.

Experimental and numerical simulation results are shown in Figs. 3 and 4. They confirm that the flow in the lower layer comprise a single roll, which occupies the entire layer. In the upper layer, the flow comprised a large roll which has a slightly skewed shape; it is thicker near the cold wall. Because of buoyancy, flow in this bulk roll has the same sense of rotation as the roll in the lower layer. An interfacial roll develops in the upper layer to satisfy the continuity conditions along the interface. This interfacial roll is relatively thick near the hot wall, and gradually reduces in thickness as it extends into the core region. Its thickness again increases near the cold wall. Horizontal extension of the recirculation into the core region is larger near the hot wall than near the cold wall. This is also confirmed by the analytical results. With increasing temperature difference, the overall interfacial roll thickness reduces. However, in the experiments the roll did not vanish up to $Gr = 240$ ($\Delta T = 20$ K), the termination point of the experiment. The reduction in thickness of the interfacial roll, although apparent, was not as clear in the experiments because the meniscus is pinned at the glass walls and does not move. Also, the numerical solutions did not reproduce the recirculation eye flow structures observed in the experiments, particulary in the lower layer (Fig. 3).

The flow structure was visualized at several locations along the depth of the cavity by moving the light sheet back and forth across the cavity. The interfacial roll thickness remained the same along the depth of the cavity. While 3-D effects cannot be completely eliminated in the experiments, and their influence cannot be completely ruled out by the above qualitative observations, it is clear from these observations that the influence of the third component of velocity in the flow-field is negligible. The observed flow structures indicate that the experimental flow is essentially 2-D.

At both side-walls, thermal boundary layers in the liquids are clearly apparent from the temperature field plots and from the interferograms. Essential features of the interfacial roll as described above are also confirmed by the interferograms, although the fringe pattern in the vicinity of the interface is somewhat blurry (due to the meniscus). At the free surface, fluid is entrained into the boundary layer at the cold wall and

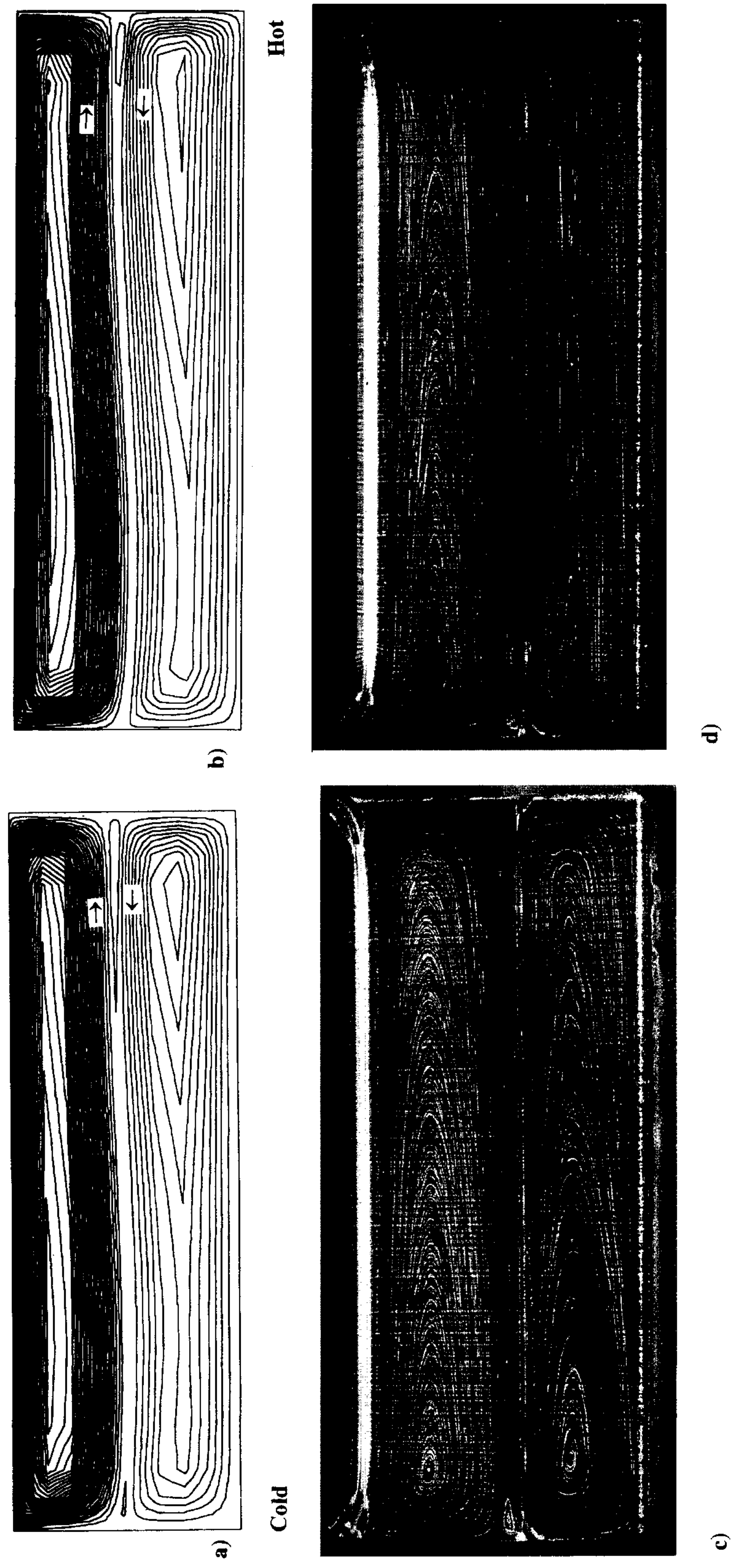

Fig. 3. Flow streamlines and streakline photographs $Bd_0 = 23.6$, $A = 0.16$; (a,c) $Gr = 24$, $\Delta T = 2$K; (b,d) $Gr = 60$, $\Delta T = 5$K.

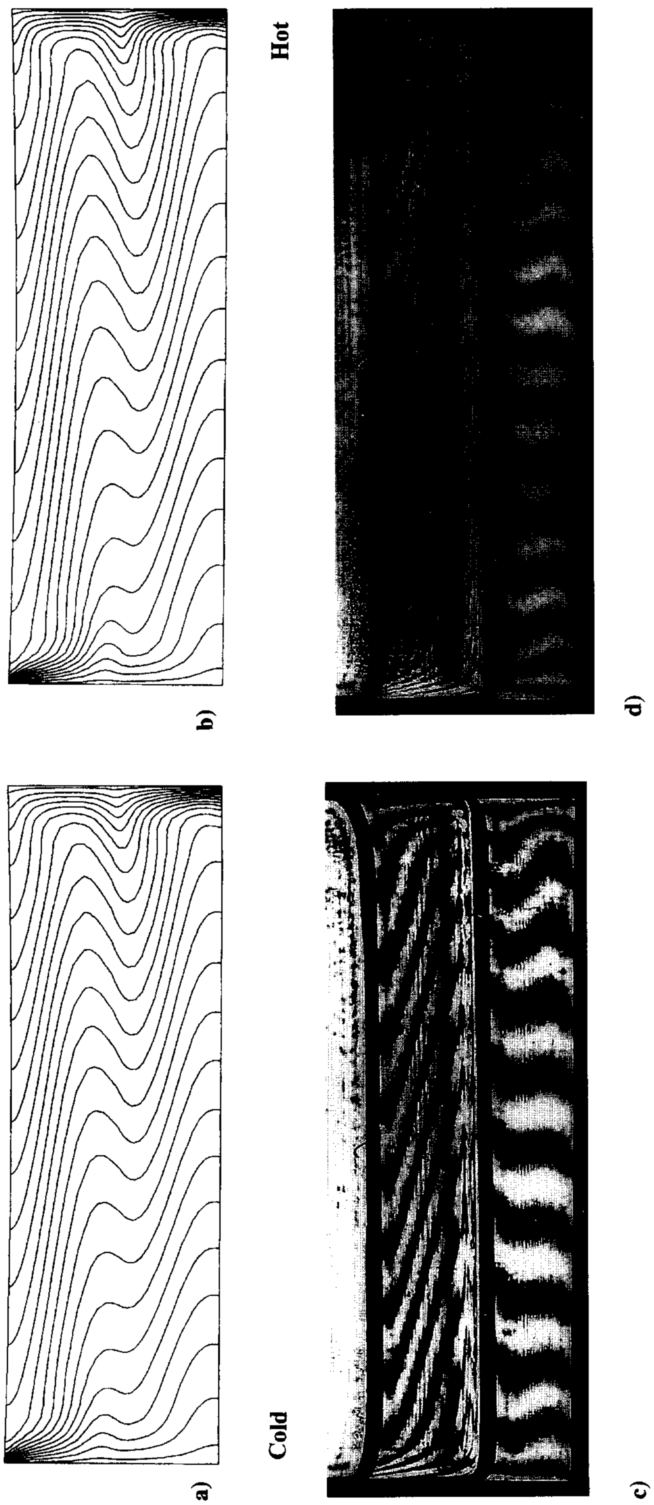

Fig. 4. Temperature contours and interferograms—$Bd_d = 23.6$, $A = 0.16$: (a) $Gr = 36$, $\Delta T = 3$K; (c) $Gr = 34$, $\Delta T = 2.9$K; (b, d) $Gr = 48$, $\Delta T = 4$K.

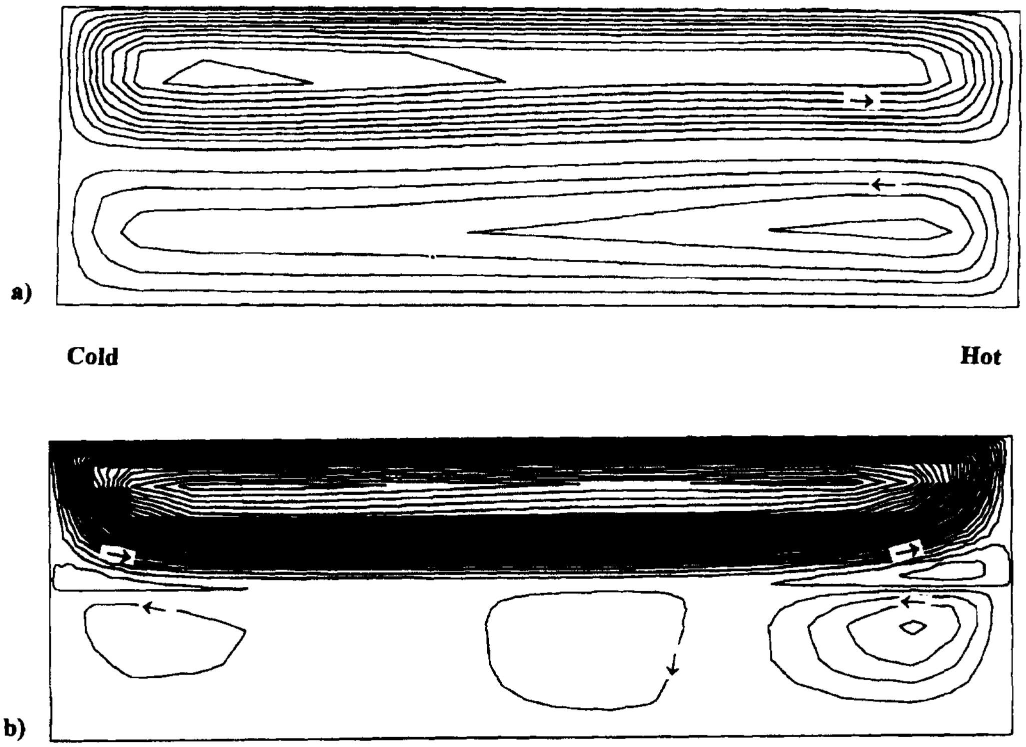

Fig. 5. Flow streamlines oil over FC-70 ($Gr = 24$, $\Delta T = 2\text{K}$, $Bd_d = 23.6$, $A = 0.16$): (a) buoyancy driven flow; (b) thermocapillary driven flow (number of contour lines doubled).

is ejected at the hot wall. The opposite is true at the bottom rigid boundary, where fluid is ejected at the cold wall and is entrained at the hot wall. The entraining regions are represented by bunched isotherms and the ejecting regions are denoted by well separated isotherms. Along the interface there is a competition between entrainment and ejection from the boundary layers in the two liquids. Such entrainment and ejection from the boundary layers has been described by Gill [2].

To determine the influence of thermocapillary stresses on the flow field, we analyzed pure buoyancy driven flow by suppressing thermocapillary stresses and pure thermocapillary flow by suppressing gravity. Results from numerical simulations of these two conditions are shown in Fig. 5(a, b). The buoyancy driven flow structure is a single roll in each layer. The fluid rises along the hot wall and descends along the cold wall. In the core region, the flow is nearly parallel to the horizontal boundaries. No interfacial roll was detected at the resolution level of the plot. The coupling occurs in an extremely thin interfacial cell.

Flow driven only by thermocapillary stresses depicts a more complex flow structure in each layer. The flow in the lower layer is almost stagnant, and is composed of two end-region thermocapillary rolls and a central roll entrained by the upper layer flow. In the upper layer, the thermocapillary shear stress along the free surface pulls liquid from the hot wall towards the cold wall. The thermocapillary shear stress along the interface also drags fluid from the hot wall toward the cold wall. The interfacial shear stress opposes the bulk flow in the upper layer. The competition between these two flows leads to the formation of interfacial rolls near the end-regions as seen in Fig. 5(b). This is due to the fact that with an increasing temperature gradient, the bulk of the applied temperature drop across the cavity happens in thin thermal boundary layer regions near the end-walls. Since the driving force for thermocapillary convection is the temperature gradient, the flow is also concentrated in the end-wall regions. It is noteworthy that flow in the two end-regions is not symmetric. Flow near the hot wall extends further into the core region than flow in the vicinity of the cold end. This asymmetry was also observed in the experiments (Fig. 3). A comparison of flow streamlines shown in Figs 3 and 4, and those shown in Fig. 5(a, b), confirms that the thickness and the flow pattern asymmetry of the interfacial roll are strongly influenced by thermocapillary stresses at the free surface and interface.

Flow pattern asymmetry is particularly noticeable in the upper layer, where the roll shape is skewed; the roll is thickest near the cold wall and gradually reduces in thickness towards the hot wall. The asymmetry can be rationalized in terms of the thermal boundary layer thickness at the two end walls. As with flow along a hot vertical plate, both the thermal and viscous

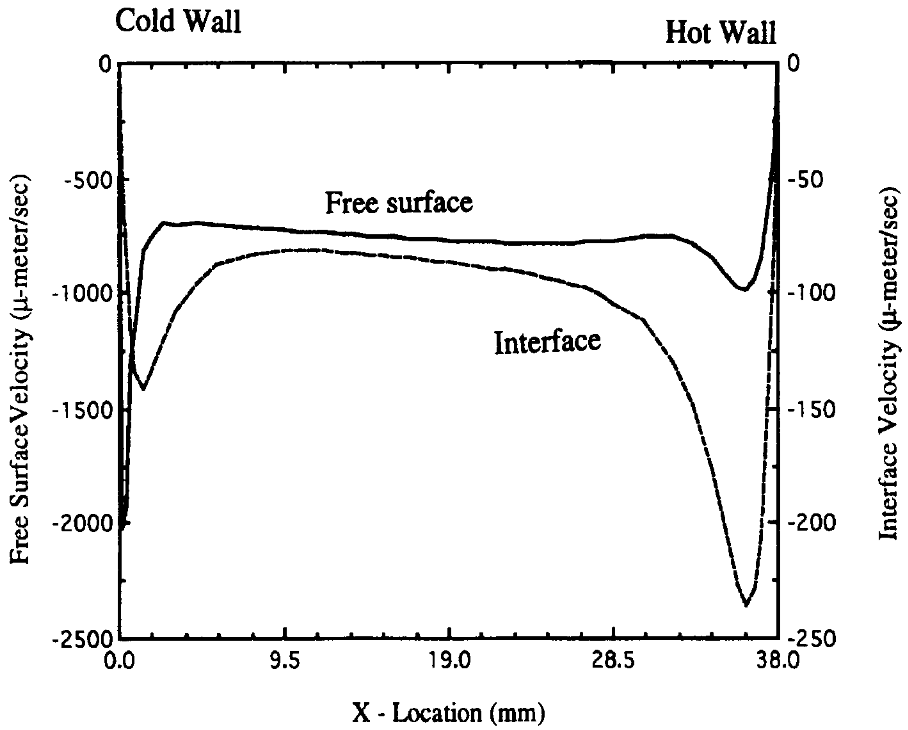

Fig. 6. Numerically computed interface and free surface velocity ($Gr = 60, \Delta T = 5\text{K}, Bd_{\text{d}} = 23.6, A = 0.16$).

boundary layers thicken with height and attain their maximum thickness at the free surface. At the free surface, the thermocapillary stress enhances the ejection of liquid from the boundary layer. This leads to an increase in the thickness of the thermal boundary layer and a further separation of the isotherms, which thereby reduces the thermocapillary stress. On the other hand, at the cold end, the boundary layer entrains fluid at the free surface and the isotherms become bunched together, reflecting a local increase in temperature gradient. As discussed by Canright [26], the thermocapillary stress further increases the thermal gradient, leading to a feedback mechanism at the cold corner. As shown in Fig. 6, the net effect is a much larger free surface horizontal velocity near the cold wall than near the hot wall. At the cold corner, this leads to a faster turning velocity and the vertical flow penetrates deeper into the bulk of the layer. At the hot wall, the turning velocity is slower and the upward extraction of fluid from the bulk does not extend as far into the layer. Thus the bulk roll attains its skewed shape.

Along the interface, the effect of the interfacial thermocapillary stress on the bottom layer buoyancy roll is similar to that described above for the free surface. The notable difference is that the bottom layer buoyancy flow combines with the interfacial thermocapillary stress to oppose the upper layer bulk flow. This leads to the formation of the interfacial roll. The strong upper layer bulk flow along the cold wall provides more resistance to the bottom layer flow and the bottom layer flow is only able to entrain a very thin region of the upper liquid. Along the hot wall, the bulk flow in the upper layer is weaker, hence entrainment by the lower layer flow extends further into the upper layer. This results in the skewed shape of the interfacial roll. Unlike the free surface horizontal velocity, the interfacial velocity attains its maximum value near the hot wall (Fig. 6).

Results of horizontal velocity measurements in the "core" region at $Gr = 60$ are shown in Fig. 7. A numerically calculated core region velocity profile is also plotted. The velocity profile in the lower layer reflects a buoyancy flow in a single layer with a sheared surface, while the upper layer profile indicates a more complicated flow, although clearly buoyancy driven. In the upper layer, the velocity profile has two zero crossings, indicating that the flow is composed of two rolls of opposite vorticity. The interfacial roll has a very small extension. It is also noteworthy that the velocity at the interface is not zero. The velocity measurements, the flow visualization and the numerical results are all in good agreement.

To ascertain the influence of the encapsulating oil layer on the fluorinert layer, the measured velocity profile in a single layer of fluorinert, without the upper encapsulating oil layer, is also included in Fig. 7. The single layer and two-layer experiments were conducted independently. Therefore, the free surface of the single layer does not exactly coincide with the interface in the two-layer case. The difference between the single layer height and the height of the lower layer

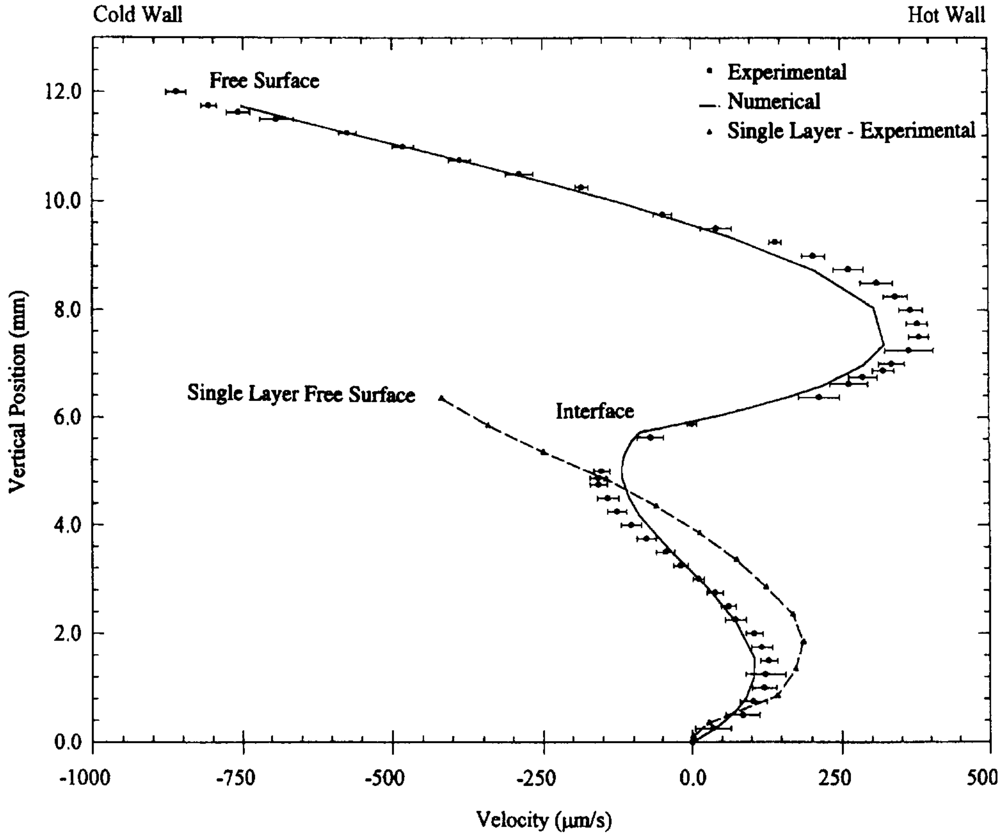

Fig. 7. Horizontal velocity profile in the core region ($Gr = 60$, $\Delta T = 5\text{K}$, $Bd_d = 23.6$, $A = 0.16$).

in the two-layer case is ~0.6 mm. A comparison of the velocity profiles shows that the oil layer has a significant influence in slowing the flow in the encapsulated fluorinert. The zero-velocity cross-over in the lower layer is also shifter vertically.

Interface and free surface horizontal velocities measured at the mid-section of the cavity, are plotted as a function of the applied ΔT in Fig. 8. The free surface velocity is notably higher than the interface velocity. The single layer free surface velocity is in between the measured free surface and interface velocities in the two-layer case. All three velocities vary linearly with applied temperature difference. Liquid encapsulation clearly reduces the flow velocity in the encapsulated layer.

CONCLUSION

Thermal convection in a two-layer system of immiscible liquids is distinguished from its single layer counterpart by the interface. Across the interface, the two liquids are mechanically and thermally coupled. In addition to buoyancy, thermocapillary stress provides a driving force for flow. From the interaction of the free surface and interface thermocapillary stress and from viscous and thermal coupling, a thin interfacial roll develops between the layers. Thermocapillary stresses tend to increase the height of the interfacial roll. The interaction of the free surface and interface thermocapillary stresses with each other and with buoyancy forces breaks the flow symmetry in both layers and the shear stress roll thickness becomes nonuniform along the width of the cavity.

Flow in the interfacial region is significantly weaker than the bulk flow and does not extend very far into the bulk of the layer. For the fluid combination considered in this study, coupling between the layers, particularly mechanical coupling, leads to a significant reduction in lower layer flow velocities as compared with the flow velocities in a single layer. For some fluid combinations, as thermocapillary stresses are reduced, the interface velocity may be very close to zero, thus the flow in the two layers would appear to be mechanically decoupled. In these cases the interfacial roll may not be observable in the experiments at all.

The experimentally observed flow and temperature fields are in good qualitative agreement with theoretical predictions from the analytical model and from the numerical simulations. The key interfacial coupling phenomena are confirmed. Experimentally measured and numerically computed velocity profiles in the "core" region of the cavity are found to be in quantitative agreement. The important contribution of thermocapillary stresses in gravitationally driven

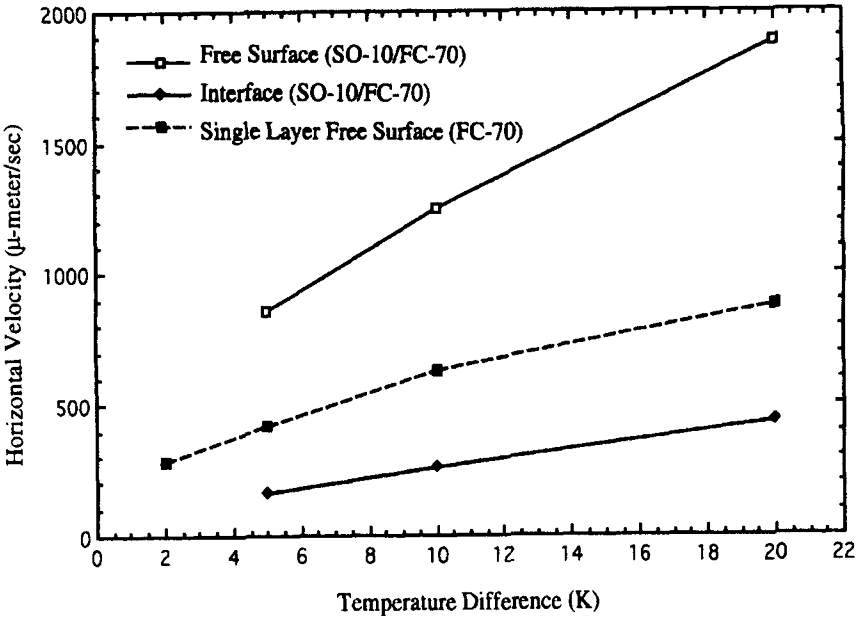

Fig. 8. Measured surface and interface horizontal velocities in the core region as a function of temperature difference.

multilayer flow has been demonstrated. This study confirms that liquid encapsulation has the potential for reducing or controlling natural convection in an electronic melt.

Acknowledgements—Support for this study from NASA under grant NAG3-1094 is gratefully acknowledged. Special thanks are extended to T. Schmidt, T. Mangold, C. V. Burkersroda for contributions that benefited the experimental efforts presented here.

REFERENCES

1. Batchelor, G. K., Heat transfer by free convection across a closed cavity between vertical boundaries at different temperatures. *Quarterly Applied Mathematics*, 1954, **XII,** 209–233.
2. Gill, A. E., The boundary layer regime of convection in a rectangular cavity. *Journal of Fluid Mechanics*, 1966, **26,** 515–536.
3. de Vahl Davis, G., Natural convection of air in a square cavity. *International Journal of Numerical Methods and Fluids*, 1983, **3,** 249–264.
4. Carpenter, B. and Homsy, G. M., Combined buoyant-thermocapillary flow in a cavity. *Journal of Fluid Mechanics*, 1989, **207,** 121–132.
5. Cormack, D. E., Leal, L. G. and Imberger, J., Natural convection in a shallow cavity with differentially heated end walls, part I, asymptotic theory. *Journal of Fluid Mechanics*, 1974, **65,** 209–229.
6. Cormack, D. E., Leal, L. G. and Seinfeld, J. H., Natural convection in a shallow cavity with differentially heated end walls, part II, numerical solutions. *Journal of Fluid Mechanics*, 1974, **65,** 231–246.
7. Imberger, J., Natural convection in a shallow cavity with differentially heated end walls, part III, experimental results. *Journal of Fluid Mechanics*, 1974, **65,** 247–260.
8. Sen, A. and Davis, S. H., Steady thermocapillary flow in two-dimensional slots. *Journal of Fluid Mechanics*, 1982, **121,** 163–186.
9. Prakash, A. and Koster, J. N., Thermal convection in a shallow cavity—part I, steady natural convection. *International Journal of Multiphase Flow*, 1994, **20**(2), 383–396.
10. Prakash, A. and Koster, J. N., Thermal convection in a shallow cavity—part II, steady thermocapillary convection. *International Journal of Multiphase Flow*, 1994, **20**(2), 397–414.
11. Villers, D. and Platten, J. K., Thermal convection is superposed immiscible liquid layers. *Applied Science Research*, 1988, **45,** 145–152.
12. Villers, D. and Platten, J. K., Influence of interfacial tension gradients on thermal convection in two superposed immiscible liquid layers. *Applied Science Research*, 1990, **47,** 177–191.
13. Ramachandran, N., Thermal buoyancy and Marangoni convection in a two fluid layered system—a numerical study. *AIAA*, #90-0254, 1990.
14. Doi, T. and Koster, J. N., Thermocapillary convection in two immiscible liquid layers with free surfaces. *Physics Fluids—Fluid Dynamics*, 1993, **5,** 1914–1927.
15. Fontaine, J. P. and Sani, R. L., High Prandtl number fluids in a multi-layered system under l-g or m-g environment. ESA-SP333, 1992, pp. 197–202.
16. Honda, S., Numerical analysis of layered convection—marginal stability and finite amplitude analyses. *Bulletin of the Earthquake Research Institute*, 1982, **57,** 273–302.
17. Zeren, R. W. and Reynolds, W. C., Thermal instabilities in two-fluid horizontal layers. *Journal of Fluid Mechanics*, 1972, **53,** 305–327.
18. Nataf, H. C., Moreno, S. and Cardin, Ph., What is responsible for thermal coupling in layered convection. *Journal of Physics France*, 1988, **49,** 1707–1714.
19. Azuma, H., Yoshihara, S., Ohnishi, M. and Doi, T., Upper layer flow phenomena in two immiscible liquid layers subject to a horizontal temperature gradient. IUTAM, 1991.
20. Durst, F., Melling, A. and Whitelaw, J. H., *Principles and Practice of Laser Doppler Anemometry*. Academic Press, London, 1981.
21. Koster, J. N., Interferometric investigation of convection in Plexiglas boxes. *Experiments in Fluids*, 1983, **1,** 121–128.

22. Farhadieh, R. and Tankin, R. S., Interferometric study of two-dimensional Bénard convection cells. *Journal of Fluid Mechanics*, 1974, **66,** 739–752.
23. Burkersroda, C., Prakash, A. and Koster, J. N., Interfacial tension between fluorinert liquids and silicone oils. *Microgravity Quarterly*, 1994, **4,** 93–99.
24. Adamson, A. W., *Physical Chemistry of Surfaces*. Wiley, New York, 1976.
25. Fluid Dynamics Analysis Package (FIDAP), Version 7.0 Users Manual, Fluid Dynamics International, 1993.
26. Canright, D., Thermocapillary convection near a cold corner. *Physics Fluids*, 1994, **6,** 1415–1424.